Nanoscale

ROYAL SOCIETY OF CHEMISTRY

COMMUNICATION

View Article Online
View Journal

Check for updates

Cite this: DOI: 10.1039/d1nr03709a

Received 9th June 2021,
Accepted 7th August 2021

DOI: 10.1039/d1nr03709a

rsc.li/nanoscale

Published on 10 August 2021. Downloaded by BNL Research Library on 9/30/2021 3:33:17 PM.

Design nanoporous metal thin films *via* solid state interfacial dealloying†

Chonghang Zhao, [a] Kim Kisslinger,[b] Xiaojing Huang,[c] Jianming Bai,[c] Xiaoyang Liu, [a] Cheng-Hung Lin, [a] Lin-Chieh Yu,[d,a] Ming Lu,[b] Xiao Tong, [b] Hui Zhong,[e] Ajith Pattammattel,[c] Hanfei Yan,[c] Yong Chu,[c] Sanjit Ghose, [c] Mingzhao Liu [b] and Yu-chen Karen Chen-Wiegart *[a]

Thin-film solid-state interfacial dealloying (thin-film SSID) is an emerging technique to design nanoarchitecture thin films. The resulting controllable 3D bicontinuous nanostructure is promising for a range of applications including catalysis, sensing, and energy storage. Using a multiscale microscopy approach, we combine X-ray and electron nano-tomography to demonstrate that besides dense bicontinuous nanocomposites, thin-film SSID can create a very fine (5–15 nm) nanoporous structure. Not only is such a fine feature among one of the finest fabrications by metal-agent dealloying, but a multilayer thin-film design enables creating nanoporous films on a wider range of substrates for functional applications. Through multimodal synchrotron diffraction and spectroscopy analysis with which the materials' chemical and structural evolution in this novel approach is characterized in details, we further deduce that the contribution of change in entropy should be considered to explain the phase evolution in metal-agent dealloying, in addition to the commonly used enthalpy term in prior studies. The discussion is an important step leading towards better explaining the underlying design principles for controllable 3D nanoarchitecture, as well as exploring a wider range of elemental and substrate selections for new applications.

Introduction

Nanoporous metals have received wide attention for their nanoscale porous structures and high surface area-to-volume ratios, leading to unique physical and chemical properties such as chemical reactivities, lightweight, and high thermal and electrical conductivities.[1–3] Dealloying is an effective method for fabricating nanoporous metals[4,5] and has led to numerous applications including catalysts,[5–8] hydrophilic substrates,[9] sensors,[10] and energy storage materials.[11–13] During dealloying, one or more components are removed from a parent alloy by a dealloying agent and the remaining components form a self-organizing bi-continuous structure.[14] Dealloying methods can be categorized based on the type of dealloying agents. The aqueous solution dealloying (ASD),[15] commonly using aqueous solutions such as acids to introduce dealloying, requires enough reduction potential differences between the elements in the parent alloy. ASD has been widely applied to fabricate nanoporous noble metals and metal oxides.[16,17] Liquid metal dealloying (LMD) method, applying a liquid metal as the dealloying agent, was reintroduced to fabricate less noble nanoporous materials to overcome the limitations of precursor element selection and to prevent the oxidation during the etching process in ASD.[18] LMD utilizes the solubility differences between the constituents of the parent alloy in the dealloying agent and has been applied to a wide range of materials, including stainless steel,[19,20] silicon,[21] magnesium,[22] graphite,[23] α-titanium,[18,24] β-titanium,[25] and TiVNbMoTa high entropy alloy.[26] Potential applications using nanoporous materials fabricated by LMD have been demonstrated, including energy storage and conversion,[27–29] environmental protection,[30] and orthopedic implants.[31] Multiscale porous metals possessing the characters of both micro- and nano-porous structures have also been developed by two-step dealloying[32,33] and by integrating the dealloying method with additive manufacturing processes.[6,34] Kinetics studies[35] and simulation[36] on morphological evolution in LMD helped to gain great insights on the dealloying mechanism and morphological evolution. Recently, solid-state interfacial dealloying (SSID), with the advantages of processing materials at a relatively lower temperature than LMD without the need to handle liquid metals, has been introduced to fabricate nanoporous Fe, Fe–Cr, α-Ti with a finer ligament size.[37–39] The SSID method was then applied to a thin-film geometry, where using

[a]*Department of Materials Science and Chemical Engineering, Stony Brook University, Stony Brook, NY 11794, USA. E-mail: Karen.Chen-Wiegart@stonybrook.edu*
[b]*Center for Functional Nanomaterials, Brookhaven National Laboratory, Upton, NY 11973, USA*
[c]*National Synchrotron Light Source II, Brookhaven National Laboratory, Upton, NY 11973, USA*
[d]*Department of Chemistry, Stony Brook University, Stony Brook, NY 11794, USA*
[e]*Department of Joint Photon Science Institute, Stony Brook University, Stony Brook, NY 11794, USA*

†Electronic supplementary information (ESI) available. See DOI: 10.1039/d1nr03709a

Published on 10 August 2021. Downloaded by BNL Research Library on 9/30/2021 3:33:17 PM.

a bulk dealloying agent[40] or a thin-film dealloying agent[39] has been demonstrated.

In the prior work of thin-film SSID, although bicontinuous metal–metal composites have been fabricated, creating a 3D bi-continuous porous structure *via* thin-film SSID has never been realized. Therefore, the advantage of fabricating fine-ligament features in thin-films by SSID has not been explored yet. Besides, the materials' design criteria for the metal-agent dealloying, especially for SSID, is not yet fully understood. The central material design criterion of the metal-agent dealloying was believed to be that one component in the parent alloy is soluble while others are insoluble in the dealloying agent. The mixing enthalpy between the soluble element in the parent alloy and the dealloying agent is expected to be more negative than the mixing enthalpy between the elements in the parent alloy. The mixing enthalpy between the insoluble element and the dealloying agent is also expected to be positive. This criterion helps to partially explain the occurrence of dealloying by LMD in some systems. However, LMD also occurs when the mixing enthalpy between the elements in parent alloys are more negative than the mixing enthalpy between the soluble element and the dealloying agent, such as in TiVNbMoTa–Ni, C–Mn, and Nb–Ni systems.[23,26,41] SSID was even reported in some systems with a positive mixing enthalpy between the soluble element in the parent alloy and the dealloying agent.[40]

In this work, we introduced thin film-SSID to dealloy Ti–Cu alloy films by Mg films and fabricated nanoporous Ti thin film with a fine (5–15 nm) pore and ligament size. The body-centered-cubic (bcc)-Ti has been reported for the first time fabricated by a dealloying process under a relatively low temperature. Its potential formation mechanisms which may be unique to thin-film-SSID were discussed. By introducing barrier and adhesion layers, we prevented undesirable morphological changes during dealloying which were associated with the thin film geometry as reported in our prior work,[39] including void formation, film dewetting, and volume expansion. The feasibility to apply thin-film SSID to different substrates were also demonstrated in this work. By applying a multimodal characterization, combining synchrotron X-ray nano-tomography and scanning transmission electron microscopy (STEM) tomography, the bi-continuous structure and its corresponding elemental distribution have been characterized in three-dimension (3D). Finally, we explored the design criteria for SSID, proposing that the contribution of the entropy should be considered together with the mixing enthalpy for the design criterion of the SSID.

Results and discussion

2D elemental distribution and quantification

A multi-layered structure was deposited on a Si substrate, and the layers are (from bottom to top): Ti adhesion layer, Ta barrier layer, Ti–Cu parent alloy layer, and Mg dealloying agent. A schematic of the thin-film SSID method to create nanoporous metal thin films is shown in Fig. 1. The cross-sectional view of the Ti–Cu layer in an as-deposited sample is shown in Fig. 2(a). Ti and Cu are homogeneously distributed within the Ti–Cu layer without any preexisting feature or phase separation. The EDX mapping confirmed the composition of the Ti–Cu film as 71.74 at% Cu and 28.26 at% Ti, which is close to the alloy composition of the sputtering target. The SEM images of the cross-sectional view of the parent alloy and dealloyed films on the Si wafers and glass slides are also shown in Fig. S1.† To save space, the sample dealloyed by Mg at 460 °C for 30 min will be noted as 460C-30, and the etched sample will be noted as 460C-30-E.

After the SSID introduced by an isothermal treatment at 460 °C for 30 min, the multilayer structure exhibits a different elemental distribution. The layers, as shown in Fig. S1(a),† are (from bottom to top): Ti adhesion layer and Ta barrier layer, both remained unchanged, and an interdiffusion Ti–Cu–(Mg) layer and a residual Mg–(Cu) layer. The dealloyed Ti–Cu layer is shown in Fig. 2(a). In the Cu and Ti EDX maps, a phase separation between Cu and Ti can be identified. In Fig. 2(b), the semi-quantitative EDX line profile indicates that the Cu concentration is close to 60 at% in the top residual Mg(–Cu) layer, and ~30 at% in the interdiffusion layer. The composition indicates that Cu and Mg may form

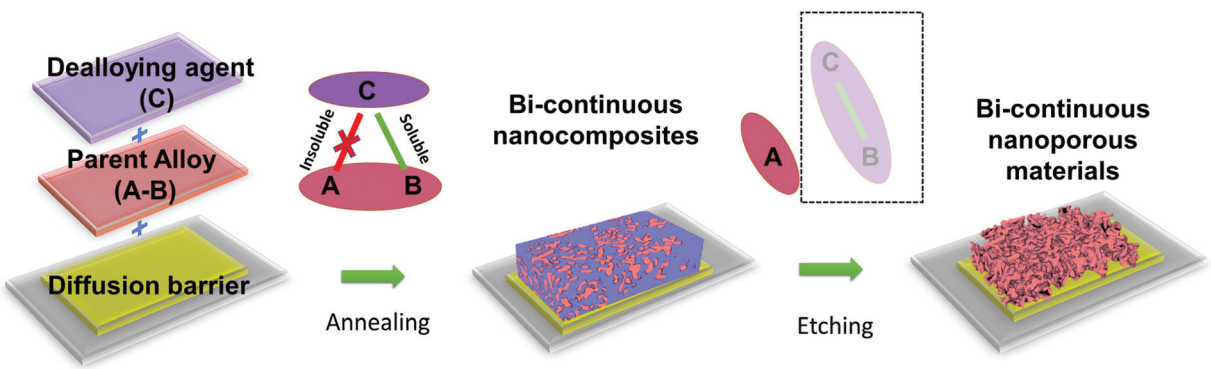

Fig. 1 Schematic of the thin-film SSID method to create bicontinuous nanoporous metal thin films.

 This journal is © The Royal Society of Chemistry 2021

Published on 10 August 2021. Downloaded by BNL Research Library on 9/30/2021 3:33:17 PM.

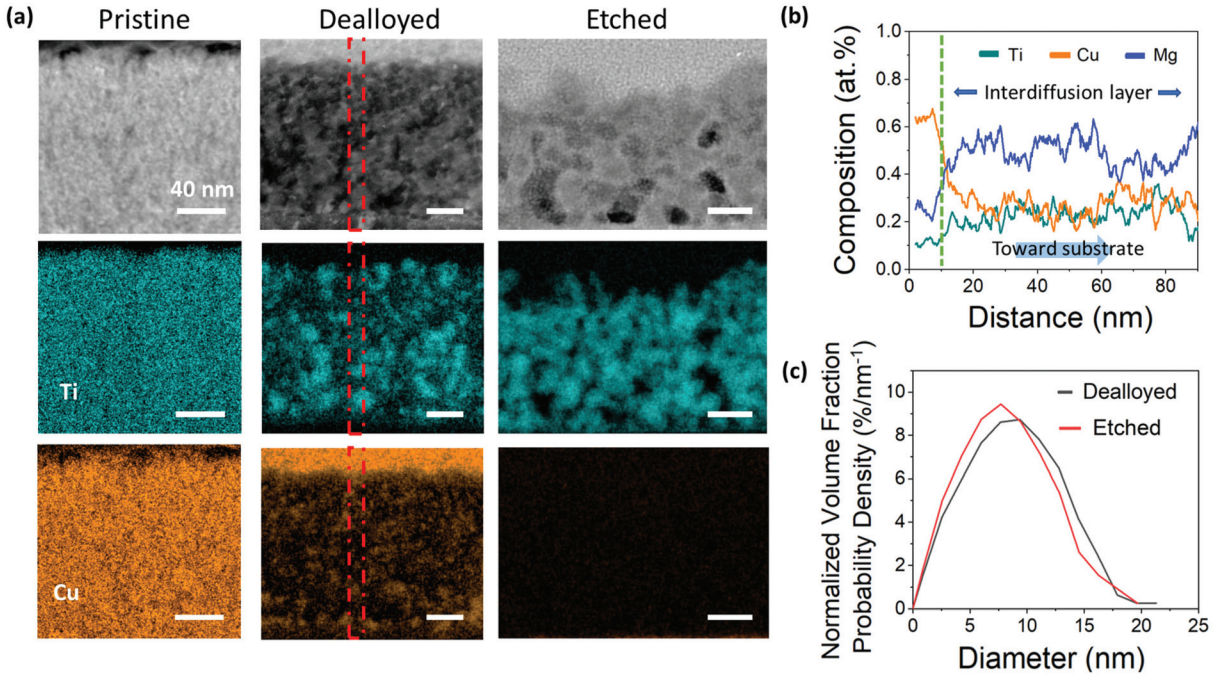

Fig. 2 Characterization of the $Ti_{30}Cu_{70}$ at% inter-diffusion layer: as-deposited, dealloyed by Mg at 460 °C for 30 min (460C-30), and etched (460C-30-E). (a) STEM characterization showing the overall morphology and the Ti and Cu elemental distribution, (b) quantitative composition analysis of Ti, Cu and Mg distribution in 460C-30 sample. The line profiles were measured from the regions in (a), as noted by the red dotted lines, and (c) ligament size distribution of 460C-30 *vs.* 460C-30-E Ti structures. (All scalebars are 40 nm.)

two different phases, Cu_2Mg and Mg_2Cu, which are consistent with the XRD analysis and will be discussed in the later section.

Mg- and Cu-containing phases were removed by the etching process, resulting in a bi-continuous nanoporous Ti structure on the Ta-/Ti-coated Si substrate, which is shown in Fig. 2(a). Note that a layer of protective Pt layer covering the nanoporous Ti structure was not part of the native sample structure and was only added as part of a standard protocol in FIB cross-sectional imaging. The ligament size distribution of the dealloyed structure before and after etching is shown in Fig. 2(c). The effect of image segmentation threshold values on the quantitative analysis is shown in Fig. S2.† The Ti ligament size before and after etching remained very similar. The resulting Ti ligament size is 5–15 nm, which is about an order of magnitude smaller of previously reported smallest ligament size by SSID (150 nm),[38] and close to the ligament size fabricated by ASD methods.[42] The ligament size is also close to nanoporous high entropy alloy (HEA) fabricated by LMD, where the atomic size difference in HEA contributed to an increased activation energy and slower rate for the surface diffusion.[26] Although anions in the etching solution can increase the surface diffusivity and lead to ligament coarsening,[43] using a very short etching time (1–1.5 s) here may have effectively prevented the coarsening of Ti ligaments. The semi-quantitative EDX mapping confirmed that the residual Cu is less than 5 at% in the etched sample, which may also include a small number of background signals from the Cu-made TEM holder.

Multiscale 3D elemental distribution

The STEM EDX tomography confirmed the phase separation of the Ti and Cu from the parent Ti–Cu alloy, which generated a relatively homogenous bi-continuous structure, shown in Fig. 3(a and b). In Fig. 3(b), a volume rendering of the Ti phase indicates that there is no ligament size gradient along the dealloying direction (top-to-bottom) within the dealloyed Ti/Cu layer, which is consistent with previous thin-film-SSID results.[39] These characters are different from prior observations in bulk structures dealloyed by LMD and SSID methods, where a simultaneous coarsening process can occur during dealloying to a larger extent due to the higher dealloying temperature (in LMD)[19] or the longer dealloying time (in bulk SSID).[37]

Previously, Shi *et al.* applied SSID to metal powders to fabricate nanoporous Ti, and fit the ligament size measured from surface SEM images as a function of dealloying temperature (~496–596 °C) with a diffusion growth model resembling grain growth.[38] However, applying this model with its fitted parameters would suggest that the size of Ti ligament dealloyed at 460 °C, as used in our current study, will be ~270 nm; this is more than 10 times larger than what was shown in our results. The significantly finer ligament in our experiment may not be completely explained by the differences in thin-film *vs.* bulk geometries. *E.g.* Sun *et al.* compared coarsening of nanoporous gold in thin films and bulk structures, and found that the onset of ligament coarsening occurred at an even lower temp-

Published on 10 August 2021. Downloaded by BNL Research Library on 9/30/2021 3:33:17 PM.

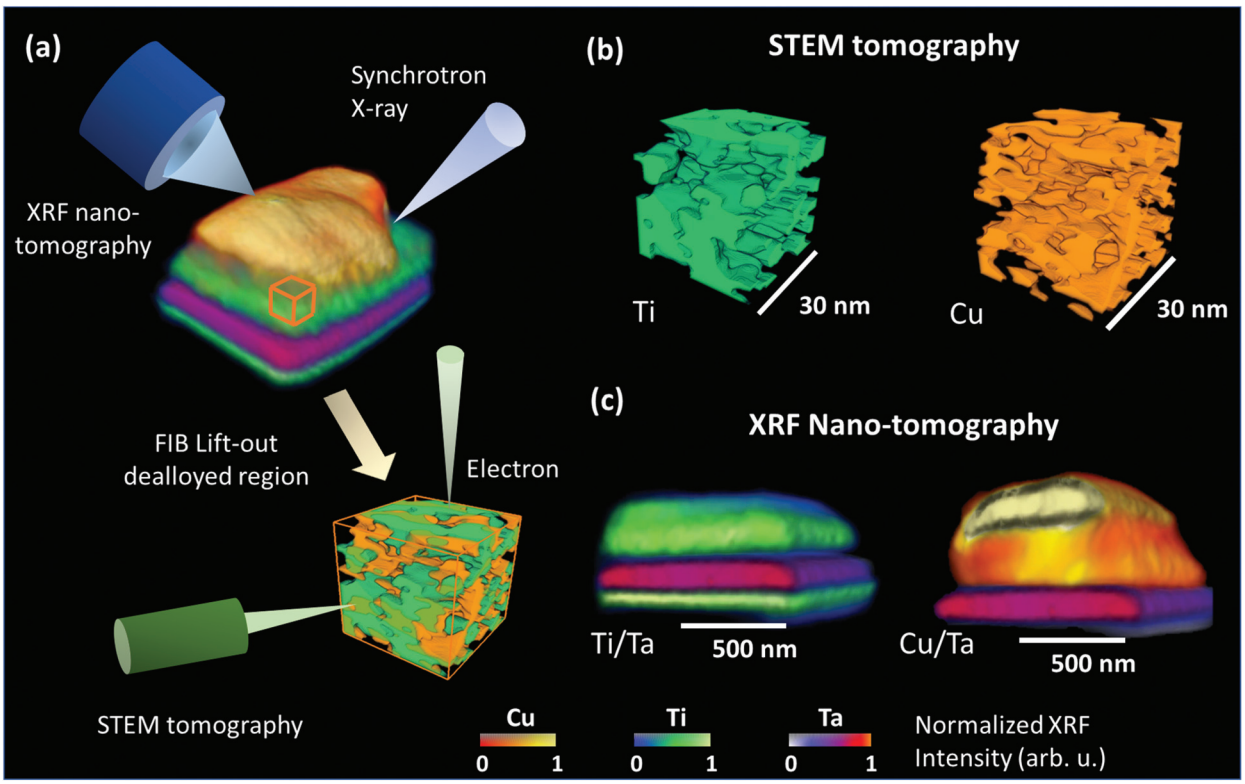

Fig. 3 A multimodal characterization by X-ray fluorescence (XRF) nano-tomography and STEM EDX tomography was carried out to analyze the 3D morphology of thin-film-SSID 460C-30 sample. (a) The multimodal characterization combining STEM and nano-probe X-ray tomography, (b) a selected volume of interest from STEM-EDX tomography showing the elemental distribution of connected Ti ligaments and Cu phases, (c) XRF nano-probe tomography of Ti/Ta/Ti layers and Cu/Ta layers. Video S1† shows the XRF nano-tomography of the 460C-30 sample, and Video S2† shows unsegmented STEM-EDX tomography of the 460C-30 sample (see ESI†).

erature in the thin films, which may be attributed to the sample geometry difference.[44]

Other factors also contribute to the smaller ligament size observed in this work. One key factor is a lower dealloying temperature used in our thin-film SSID process. In the previous study, porous Ti was fabricated *via* SSID at a temperature higher than the Mg–Cu eutectic point of 485 °C; this led to a phase transformation of Mg–Cu alloys from the solid to the liquid state.[38] In contrast, the temperature in our experiment is lower than the eutectic point of Mg–Cu. An additional factor influencing the ligament size may be the surface oxidation of Ti. The oxides on the surface of ligaments promote the creation of adatoms and vacancies at the step edge, which significantly limits the surface diffusion during the coarsening process, leading to a finer ligament size.[43] Similarly, coating the surface of nanoporous gold with TiO_2 or other oxides to increase thermal stability has been reported previously.[45,46] As a non-noble porous metal, Ti would naturally develop titanium oxide on the surface. XPS and XANES analysis (presented in the next section in Fig. 4) indicates that a small number of titanium oxide is present in the dealloyed samples, which may explain the small ligament size. Overall, the small number of surface oxides can provide dual-functionality – chemical reactivity as oxides for applications such as catalysts and energy storage, as well as a surface diffusion barrier that inhibits coarsening.

The results from 3D XRF nano-tomography of the dealloyed sample are shown in Fig. 3(a) and (c). The relatively higher penetration depth of X-ray compared to the electron beam in STEM EDX tomography enabled imaging of the entire system, which contains multiple layers. All the layers include (from bottom to top): Ti adhesion layer, Ta barrier layer, dealloyed Ti–Cu–(Mg) layer, and residual Mg(–Cu) layer. Strong Cu fluorescence signals from the very top layer indicate that much Cu has diffused into the Mg dealloying agent layer. This is consistent with the STEM cross-sectional image and tomography results shown in Fig. 2(b). Note that no Cu was found within or below the Ta barrier layer, which demonstrates that Ta is an effective barrier layer for Cu. Besides, the interfaces between the Ta layer and the adjacent layers – dealloyed Ti layer on the top and the adhesion Ti layer on the bottom – are also sharp, indicating no interdiffusion between Ta and Ti. The barrier layer is important in the thin-film-SSID process. In the Ti–Cu SSID, diffusion of Cu into the Si substrate could lead to a significant volume expansion and structural failure, as shown in Fig. S4.† Ta has been demonstrated as an effective barrier layer between Cu and Si wafer up to 600 °C.[47] In our system, although Ta is miscible with Ti, the inter-diffusivity between Ti

 This journal is © The Royal Society of Chemistry 2021

Published on 10 August 2021. Downloaded by BNL Research Library on 9/30/2021 3:33:17 PM.

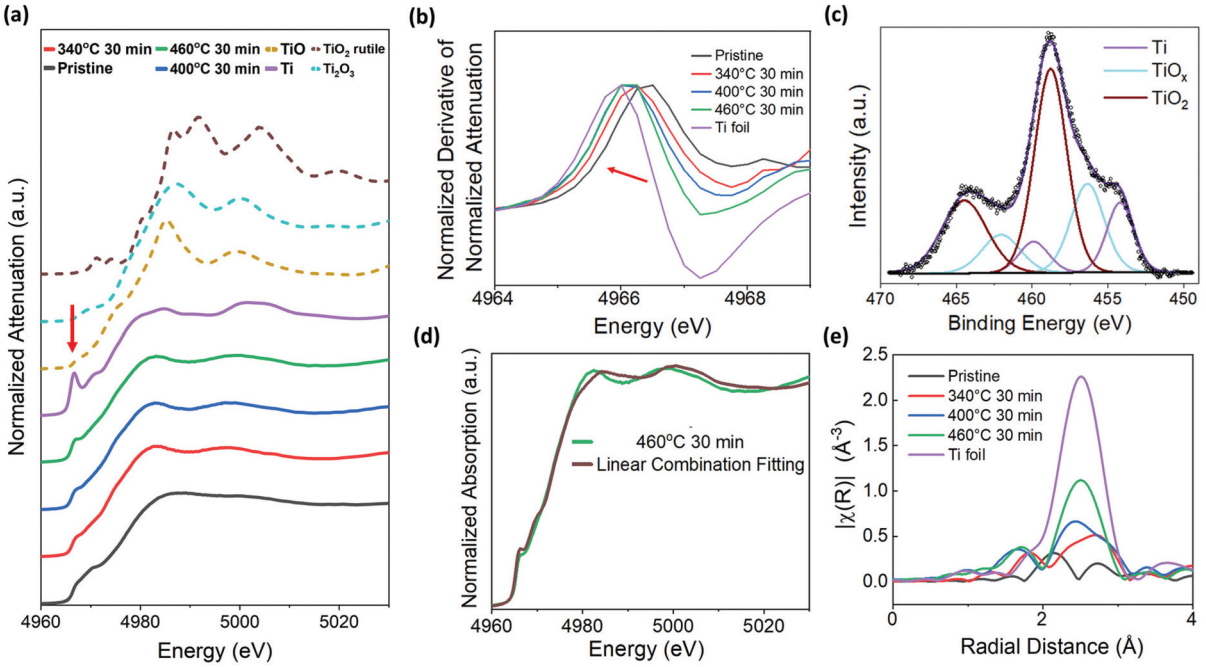

Fig. 4 Compositional analysis of parent-alloy and dealloyed films by X-ray absorption near edge spectroscopy (XANES), X-ray photoelectron spectroscopy (XPS) and extended X-ray absorption fine structure (EXAFS): pristine $Ti_{30}Cu_{70}$ at%, sample dealloyed at 340 (340C-30), 400 (400C-30) and 460 °C (460C-30) for 30 min: (a) XANES analysis of the samples compared with standards Ti, TiO, Ti_2O_3 and TiO_2, with an arrow indicating the pre-edge feature. (b) The first derivative of XANES spectra quantified the edge shift. (c) XPS analysis of Ti 2p on 460C-30 sample, after sputtering by Ar^+ at 1.5 keV for 300 min. (d) The linear combination fitting of the 460C-30 sample. The data was fitted with $Ti_{10}Cu_{90}$ pristine, $Ti_{90}Cu_{10}$ pristine, $Ti_{30}Cu_{70}$ pristine, Ti foil, TiO, Ti_2O_3, TiO_2 rutile, and the best fitting result is the combination of pure Ti (40.0 wt%) and $Ti_{90}Cu_{10}$ pristine (59.1 wt%). (e) Fourier transform magnitude of k-weighted EXAFS on the pristine, 340C-30, 400C-30, and 460C-30 samples.

and Ta is several orders of magnitude lower than that between Ti and Cu,[35] such that introducing Ta will have a very limited impact on the SSID system and it could still be used as an effective barrier layer.

Compositional and structural evolution

The chemical composition of the pristine and dealloyed $Ti_{30}Cu_{70}$ at% samples were characterized by X-ray absorption near edge spectroscopy (XANES), shown in Fig. 4(a). Their spectra were compared with various Ti compound standards, including Ti, TiO, Ti_2O_3, and TiO_2. The Ti K-edge XANES spectra from the dealloyed samples are similar to the one from the pure Ti. The intensity of a pre-edge feature gradually increases from the pristine to the samples dealloyed at higher temperatures, as indicated by an arrow in Fig. 4(a). This pre-edge feature corresponds to a quadrupole transition from the 1s core state to 3d states and is related to the symmetry of transition metals.[48] The increasing pre-edge feature indicates that the Ti coordination gradually changes from an alloy to a pure Ti. The first derivatives of the spectra from all the samples and pure Ti are shown in Fig. 4(b). The maximum on the first derivative curves corresponds to the absorption edge. The edge shifts towards a lower energy, closer to the edge position of a pure Ti, which can be observed as a function of dealloying temperature. This also corresponds to the XPS result in Fig. 4(c) that a small amount of Ti oxides distribue within the sample. Linear combination analysis of the XANES spectra showed that the 460C-30 samples are composed of 40.0 wt% of pure Ti and 59.1 wt% of $Ti_{90}Cu_{10}$ alloy, which is shown in Fig. 4(d). This indicates that the dealloying process has partially separated the Ti phase from the Cu phases, with some amount of $Ti_{90}Cu_{10}$ alloy that has not fully dealloyed. A longer dealloying time will likely be needed to create a fully dealloyed Ti–Cu. The Fourier transform of the EXAFS spectra (Fig. 4(e)) shows that the positions of the first nearest-neighbor peaks of 460C-30 samples and Ti foil are in a good agreement. This first nearest-neighbor peak corresponding to the Ti–Ti bond. The trend of an increasing magnitude of Ti–Ti bond from pristine to 460C-30 samples indicates the crystallization from amorphous Ti–Cu phase to crystalline Ti during dealloying process.[49,50]

The crystal structures of the pristine and dealloyed $Ti_{30}Cu_{70}$ at% samples were analyzed by synchrotron X-ray powder diffraction (XRD), shown in Fig. 5(a). The XRD pattern of the pristine sample only exhibits diffraction signals from Mg, indicating that only the Mg film was crystalline, whereas the Ti–Cu and Ta thin films were amorphous. After the dealloying process induced by the isothermal treatment, the crystalline Cu_2Mg and $CuMg_2$ phases were identified in the system, which is also consistent with the EDX analysis as discussed in the prior section, as well as prior Cu–Mg interdiffusion studies.[51] The results indicate that a phase separation between

Published on 10 August 2021. Downloaded by BNL Research Library on 9/30/2021 3:33:17 PM.

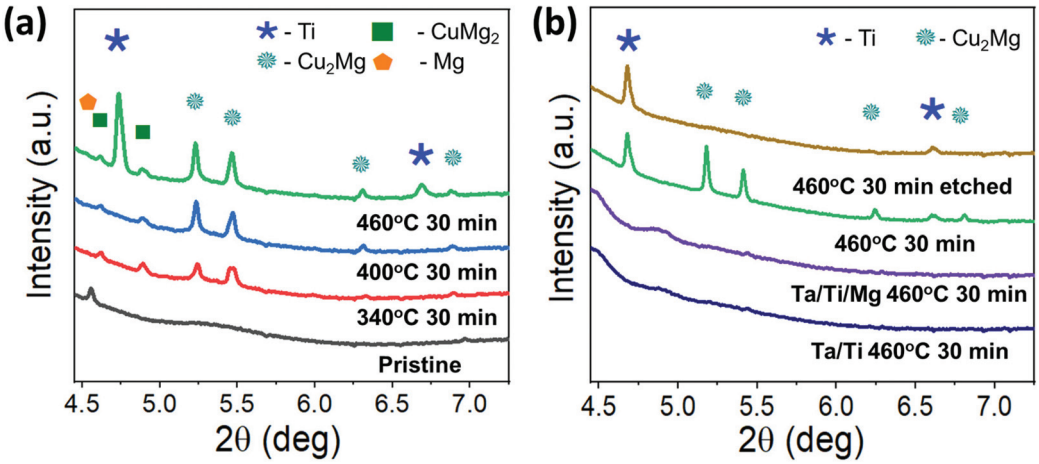

Fig. 5 Structural analysis of parent-alloy and dealloyed films by X-ray diffraction. (a) X-ray diffraction analysis with phase identification. (b) X-ray diffraction analysis on additional controlled samples: Ta/Ti-460C-30 and Ta/Ti/Mg-460C-30, compared with the 460C-30 and 460C-30-E samples.

Ti–Cu occurred, as well as an inter-diffusion between the Cu and Mg, further confirming the dealloying of Ti–Cu driven by the Mg phase. No diffraction peaks from Ti_xCu intermetallic phases were identified from dealloyed samples. This is consistent with the thermodyanmics of the system, of which the activation energies of Ti_xCu phase crystalization are in range of 261–303 kJ mol^{-1},[52] while the activation energies for growths of $MgCu_2$ and Mg_2Cu phases, which are ~139.1 and ~147.6 kJ mol^{-1}.[53] The dealloying process of the Ti–Cu alloy, leading to the phase separation and formation of crystalized Cu_xMg, is thus favorable than the parent alloy crystalization.

Moreover, three new diffraction peaks were identified from XRD analysis of the 460C-30 sample, which can be attributed to either the Ta phase in the barrier layer or a bcc-Ti phase in the dealloyed layer based on the peak locations. The Cu_2Mg and $CuMg_2$ phases were removed from the 460C-30-E sample; the XRD pattern from the etched sample also confirmed that there are no Cu_2Mg or $CuMg_2$ diffraction peaks, while the potential Ta or bcc-Ti phase remains, as shown in Fig. 5(b). Note that these potential Ta or bcc-Ti XRD peaks are only present in the data corresponding to 460 °C dealloying, and not in those corresponding to 340 °C and 400 °C dealloying conditions, indicating that this crystalline phase formation did not occur at a lower dealloying temperature, which is also consistent with the Fourier transform of EXAFS data as discussed in the previous section.

To identify whether these three peaks are associated with the Ta or the bcc-Ti phase, several control samples were characterized, including sputtered thin film samples with double Ta/Ti layers and triple Ta/Ti/Mg layers. These control samples were also heat-treated at 460 °C for 30 min, and their XRD analysis results are shown in Fig. 5(b). However, in the absence of Ti–Cu parent alloy, no diffraction peak can be found from any of these controlled samples, indicating that the diffraction peaks cannot be attributed to the Ta barrier layer. Therefore, the three new diffraction peaks are likely from the dealloyed structure, indicating a formation of bcc-Ti from dealloying.

Here, we briefly discuss potential bcc-Ti formation mechanisms. The thin film geometry and energy delivered by the particle bombardment in the sputtering deposition process can influence bcc-Ti formation. Liu *et al.* reported that a formation of bcc-Ti by the deposition of Ti–Mo alloy thin films can be realized at a much lower temperature than bulk Ti–Mo structure.[54] However, no diffraction was detected from controlled Ta/Ti-460C-30 and Ta/Ti/Mg-460C-30 samples. The formation of bcc-Ti may not be directly related to the presence of bcc stabilizing elements in the system, such as Ta, Cu and H. Ta is a good isothermal bcc stabilizing element, but the critical concentration of Ta to stabilize binary Ti alloy at room temperature is 45 at%.[55] However, no diffraction peak was identified in the heated bi-layer Ta/Ti control sample, and the interdiffusion between Ta and Ti was not identified by the 3D XRF nano-tomography shown in Fig. 3. H is an eutectic bcc stabilizing element and can form bcc-Ti at a much lower temperature.[56] However, no diffraction peak was identified in the heated Ta/Ti bi-layer samples, which means that heating Ti films in the 4% H_2 environment were not enough to introduce a bcc-Ti formation. Cu may be related to the bcc-Ti formation. Since the bcc structure has been found in CuTi, $CuTi_3$, Cu_3Ti_2, and Cu_4Ti_3,[57] it is possible that the bcc structure in the parent alloy was preserved in the dealloyed structure, which is common in chemical dealloying methods. However, no Ti–Cu intermetallic crystalline phase was identified in the pristine film base on the diffraction analysis. Alternatively, the formation of bcc-Ti may be related to the presence of Mg; a bcc $Mg_{1-y}Ti_y$ ($0.25 < y < 0.65$) formation has been reported in the literature: one case in a spark discharge generation process followed by rapid quenching, and another case in ball milling synthesis.[58,59] The atomic-scale intermixing of Ti and Mg was achieved in Mg–Ti nanoparticles reported by Anastasopol *et al.* with an 11 ± 2 nm diameter. In comparison, here we dealloyed

 This journal is © The Royal Society of Chemistry 2021

Published on 10 August 2021. Downloaded by BNL Research Library on 9/30/2021 3:33:17 PM.

the Ti from the Ti–Cu alloy and generated 5–15 nm Ti ligaments. However, there is no overlap in Ti and Mg signals in the EDX mapping analysis, as shown in Fig. S5,† thereby we confirmed that Mg and Ti did not form an alloy in the sample. This is consistent with the design of the SSID system, in which Ti and Mg should remain insoluble during SSID. XRD analysis of the heated Ta/Ti/Mg tri-layer sample further confirmed that a very limited interdiffusion between Mg and Ti cannot support the formation of bcc Ti films.

Design criteria for SSID

Prior studies generalized the criteria of dealloying by a metallic agent (LMD and SSID) as the following: the mixing enthalpy between the soluble element and the dealloying agent needs to be more negative than the mixing enthalpy between the elements in the parent alloy. However, in the Ti–Cu–Mg system, the mixing enthalpy between Ti–Cu (the parent alloy) is −9 kJ mol^{-1} while Cu–Mg (the soluble element and dealloying agent) is −3 kJ mol^{-1}.[60] If only the mixing enthalpy is considered here, the Cu would have a stronger tendency to remain mixed with the Ti, rather than being dealloyed to mix with the Mg. Other thermodynamic properties such as entropy thus also need to be considered.

In the LMD, dissolving Cu from an alloy into a liquid Mg will increase entropy, such that the total free energy will reduce during the dealloying process, resulting in the dissolution of Cu. In SSID, we may also consider the influence of entropy. In binary solid solution, density functional theory calculation indicates that vibrational and configurational entropy can together contribute to binary phase stability or instability, which explains that there are stable binary systems with a positive mixing enthalpy.[61] In binary intermetallics, the configurational entropy in a binary system can be very small when being compared to the solid solution; however, the excess configuration contributed by the atom arrangement, atom size, atomic vibration, magnetic moment, and electronic effect make an important contribution to the total entropy.[62] Here we briefly discuss the increase of excess entropy that induced by different atomic size in parent alloy and dealloying agent. The different atom sizes can bring uncertainty in atomic positions, which leads to an increase in the excess entropy.[62] In all previous SSID studies, the difference of atomic size between the dealloying agent and the soluble element is larger than the difference between the elements within the parent alloys, as summarized in Table S1.†[37–40,63] This difference may lead to a driving force for the SSID to occur due to this increase of entropy within the system.

In addition, while the calculated enthalpy by Miedema's method could provide a guideline for the prediction of dealloying, the deviation of the calculated enthalpy from the experimental results in the liquid state can be as high as ±50%.[62] Feufel *et al.* reported that the enthalpy of mixing in $CuMg_2$ is −9.8 ± 1.8 kJ mol^{-1}, and in Cu_2Mg is −12.7 ± 2.0 kJ mol^{-1}, contradicting to the prediction from the Miedema's model for Cu–Mg, which is −3 kJ mol^{-1}. Thus, the experimental mixing enthalpy between Cu and Mg can be more negative than that between Ti and Cu, which differs from the calculation by the Miedema's method.[64]

In summary, although mixing enthalpy values calculated by Miedema's method provide a guide for predicting dealloying systems, the contribution of entropy to the occurrence of SSID should also be considered, especially when a solid solution form within dealloying systems. Moreover, mixing enthalpy values calculated by Miedema's method should also be carefully checked against experimental values before determining dealloying systems. The criteria of dealloying by metal agents should be updated correspondingly, especially considering the solid-state dealloying: the free energy of mixing should be greater in the solvent than in the parent phase.

Conclusion

Thin-film solid-state interfacial dealloying (thin-film SSID) as a new method to fabricate a 3D bi-continuous porous structure was demonstrated for the first time. The pore and ligament sizes fabricated by the thin-film SSID were in the range of 5–15 nm, close to the smallest ligament size fabricated by the aqueous solution dealloying method, and dealloyed high-entropy alloys by liquid metal dealloying method. Thin-film-SSID shows a potential to create high surface area metal/metal oxides with high thermal stability and a high chemical reactivity with a small ligament size. By introducing barrier and adhesion layers, we prevented morphological changes and substrate interactions due to the thin-film geometry, previously observed in thin-films-SSID.

A multimodal microscopy approach was used to analyze the 3D morphology of the dealloyed film from the nm to μm length scale. The dealloyed bi-continuous structure was characterized by a high-resolution STEM-EDX tomography. In addition, X-ray fluorescence nano-tomography demonstrates that the barrier layer can effectively prevent undesired interdiffusion between the thin films and the substrate.

A small number of titanium oxides can be found in dealloyed thin films, which could potentially provide dual-functionality – chemical reactivity as oxides for applications such as catalysts and energy storage materials, as well as a surface diffusion barrier that inhibits coarsening. The formation of nanoporous bcc-Ti by dealloying at a relatively low temperature (460 °C) was reported for the first time. The potential formation mechanisms of the bcc-Ti were discussed, including the influence of a thin film geometry and an interdiffusion between constituent elements.

By analyzing the mixing enthalpy and the atomic size differences in SSID systems, we explore the design criteria for SSID. In addition to the commonly used enthalpy criterion, we proposed to also include the entropy term into the consideration for SSID. The different atomic sizes between the parent alloy and the dealloying agent element may induce entropy changes, leading to the occurrence of the SSID. This consideration is particularly important when a solid solution forms after dealloying, in which using the mixing enthalpy as the

Published on 10 August 2021. Downloaded by BNL Research Library on 9/30/2021 3:33:17 PM.

dealloying criterion would not be sufficient. Overall, a novel way of fabricating nanoporous metal at a relatively low temperature compared with liquid metal dealloying was demonstrated with discussions on the design criteria of SSID, paving the way towards designing a wide range of nanoporous metal thin films for applications using the SSID method.

Experimental section

Silicon (Si) wafers (University Wafer, ⟨100⟩) were cut to 1 × 1 cm^2 square size and used as deposition substrates. In addition, borosilicate glass slides (TedPella) with an area of 1 × 1 cm^2 and a thickness of ~170 μm were used as deposition substrates for X-ray diffraction and X-ray absorption measurements to avoid the Bragg diffraction from the Si substrates. Before deposition, the wafers and glass slides surface were cleaned by isopropyl alcohol, de-ionized water, and followed by an oxygen-plasma cleaning treatment. Ti (99.995% purity from Kurt J. Lesker) and Ta (99.95% purity from Kurt J. Lesker) thin films were deposited by sputtering as an adhesion layer and a barrier layer. $Ti_{30}Cu_{70}$ at%, and Mg sputtering targets (both 99.95% purity from Stanford Advanced Materials) was used to deposit the Ti–Cu parent alloy and Mg dealloying agent thin films. For each sputtering target, a cleaning protocol was followed to remove the surface oxides by sputtering the target for 5–10 min with the sputtering shutter closed.

Ti, Ta, Ti–Cu, and Mg thin films were sequentially sputtered onto the Si wafer substrates. The thickness of each layer is ~40 nm for Ti, ~80 nm for Ta, ~120 nm for Ti–Cu, and ~300 nm Mg. To avoid the influence of Ti adhesion layer onto the X-ray analysis of the Ti phase in the dealloying process, Ta, Ti–Cu, and Mg films were deposited onto borosilicate glass slides. The films' thickness was also increased such that a stronger diffraction signal can be detected for structural analysis, with ~80 nm Ta, ~300 nm Ti–Cu, and ~500 nm Mg.

After deposition, samples were heated by the rapid thermal processing (Modular Process Technology Corp.) method for an isothermal heat treatment to introduce dealloying. All the heat treatment processes were conducted in a reduced gas atmosphere (4% hydrogen and 96% Argon) to prevent oxidation during the heat treatment. Samples were heated from room temperature to the designated dealloying temperature in 30 s and kept at the dealloying temperature for a designated duration. The samples were then cooled down to room temperature in ~150 s. The heating temperature was set to be lower than the Mg melting temperature and the eutectic point of the Cu–Mg phase, so that dealloying occurs in a solid state. The heating temperature and time for both types of samples were determined based on the estimated diffusion length calculated from the diffusion data in the literature.[65] After dealloying, the residual Mg–Cu was removed by emerging the dealloyed film in an etching solution CE-200 (Transgene, with a composition of 25–35 wt% $FeCl_3$, and 3–4 wt% HCl) for ~1 s. Etched samples were then thoroughly rinsed in deionized water for 5 min and dried with N_2 gas.

A focused ion beam with scanning electron microscopy (FIB-SEM, Helios dual beam, FEI) was used to obtain SEM images for cross-sectional morphological analysis, to prepare samples for STEM analysis, and to prepare X-ray nano-probe tomography samples. The STEM lamella sample was prepared by following a standard sample preparation procedure to create a thin lamella with a thickness less than 100 nm for electron transparency. The STEM/Energy-dispersive X-ray spectroscopy (EDX) tomography sample was prepared by milling the sample to create a cylindrical shape with a diameter of less than 200 nm and a length of 2 μm. The X-ray nano-probe tomography sample was milled to a cylindrical shape with a diameter of 1 μm and a length of 4 μm following an established procedure.[66]

STEM characterization was carried out in a S/TEM (Talos model, FEI), operating at 200 keV. High-angle annular dark-field imaging (HAADF) and EDX analysis were conducted to study morphology and elemental distribution. The EDX tomography sample was collected at a 2° angular step size, with a total of 120° angular range (60 STEM-EDX images). The exposure time for each image was 300 s. The FIB-SEM and STEM-EDX analysis were conducted at the Center for Functional Nanomaterials (CFN, Brookhaven National Laboratory).

3D X-ray fluorescence (XRF) nano-tomography was conducted at the Hard X-ray Nanoprobe (HXN) beamline 3-ID at the National Synchrotron Light Source II (NSLS-II), Brookhaven National Laboratory. XRF images were collected at a 1.5° angular step size, with a total of 120 XRF images in a 180° angular range. A multilayer Laue lens with an optical resolution of 10 nm was used for focusing the X-ray beam onto the sample.[67] The scanning area of each image was 1.1 × 1.1 μm^2 with a 10 nm step size. The fluorescence spectra were collected with a dwell time of 30 ms for each scanning point. The incident X-ray beam energy was 12 keV, above the Ti and Cu K edges, and the Ta L edge. The XRF fitting was conducted using a PyXRF package.[68]

The alignment of STEM-EDX and XRF images was conducted using an automatic cross-correlation algorithm in Tomviz software (for STEM images)[69] and ImageJ[70] with a plugin MultiStackRegistraion (for XRF images),[71] both with further manual alignment correction. TomoPy, a Python-based package was used for image reconstruction for both STEM-EDX and XRF nano-tomography.[72] The Ti and Cu phases in reconstructed EDX images were segmented using a trainable Weka Segmentation,[73] a machine learning algorithm in ImageJ. Matlab codes developed in-house by a previously established method were used to quantify feature size distribution, based on the segmented two-dimensional STEM-EDX images.[74] The volume rendering and visualization of the tomographic data were carried out using Avizo software (*v.*9.0 FEI).

X-ray photoelectron spectroscopy (XPS) characterization was conducted in an ultrahigh vacuum (UHV) system with a base pressures $<2 \times 10^{-9}$ Torr. The XPS instrument was equipped with a hemispherical electron energy analyzer (SPECS, PHOIBOS 100) and a twin anode X-ray source (SPECS, XR50).

 This journal is © The Royal Society of Chemistry 2021

Published on 10 August 2021. Downloaded by BNL Research Library on 9/30/2021 3:33:17 PM.

The characterization followed a standard XPS characterization protocol.[75] Al Kα (1486.6 eV) radiation was used at 10 kV and 30 mA. The angle between the analyzer and X-ray source was 45°, and photoelectrons were collected along the sample surface normal. To determine the chemical states of Ti, the surface Mg–Cu layer was removed by Ar^+ ion sputtering with a 1500 V beam voltage.

X-ray diffraction analysis was conducted at X-ray powder diffraction (XPD) beamline 28-ID at NSLS-II (Brookhaven National Laboratory). The incident X-ray beam energy was ~63.6 keV, with a corresponding X-ray wavelength at 0.19316 Å and 0.1949 Å for two different beamtime measurements. The beam size was 0.5 mm × 0.5 mm. A large-area X-ray detector with 2048 × 2048 pixels was used to collect the diffraction patterns, and the size of each pixel was 200 × 200 μm^2. The distance from the sample to the detector was first calibrated with a Ni standard and determined to be 1378.43 mm. The phase identification based on the XPD results was carried out by comparing the peak locations with references using a commercial software packages Jade (Materials Data, Inc.).

X-ray absorption near edge spectroscopy (XANES) at Ti K-edge spectra was conducted at the Beamline for Materials Measurement (BMM, 6-BM) at NSLS-II (Brookhaven National Laboratory). XANES spectra were collected from samples with glass substrates in a fluorescence mode at a glancing angle of 3°. The Ti foil and Ti(II)O (Sigma Aldrich), $Ti(III)_2O_3$ (Sigma Aldrich), $Ti(IV)O_2$ rutile (Sigma Aldrich) powder standards were measured in a transmission mode. Eight scans were collected and averaged for each sample to improve the signal-to-noise ratio. The XANES spectra were analyzed by Athena package, including averaging, background correction, normalization, and linear combination analysis (LCA).[76] LCA was used to fit the XANES region (energy range of 4940 eV–5010 eV) using $Ti_{10}Cu_{90}$ at% pristine, $Ti_{90}Cu_{10}$ at% pristine, $Ti_{30}Cu_{70}$ pristine, Ti foil, TiO, Ti_2O_3, TiO_2 rutile as references. Fourier transform was then conducted for the EXAFS analysis. The energy was calibrated to the first derivative peak in metallic Ti at 4966 eV. Linear regression was conducted to fit the pre-edge region and a quadratic polynomial was used to fit the post-edge region. The background was removed and the data were assigned with an Rbkg value (1.0–1.8) to reduce the low-radial distance component in Fourier transform. Fourier transform of k^2-weight EXAFS spectra was analyzed over a range of 2–10 $Å^{-1}$ in k-space with dk = 2.

Author contributions

Y.-c. K. C.-W., and Mingzhao L. and C. Z. developed the research idea. Y.-c. K. C.-W. and C. Z. wrote user proposals for the use of HXN, XPD and BMM beamlines at NSLS-II and equipment at CFN. C. Z. conducted thin film deposition under the training and direction of Ming L. and Mingzhao L.; C.-H. L. provided valuable advice on the thin film deposition process. C. Z. conducted an RTP heating process under the training and direction of Mingzhao L.; K. K. conducted a TEM tomography sample preparation by FIB-SEM and EDX/STEM analysis, with the participation of C. Z. and X. L.; C. Z. conducted STEM-EDX tomography reconstruction and quantitative analysis on STEM images. C. Z. conducted FIB-SEM for additional sample preparations for SEM, TEM and XRF tomography samples. X. H., A. P., H. Y. and Y. C. setup the HXN beamline and provided user support for the experiment. C. Z. prepared HXN sample. C. Z., X. H. and Y.-c. K. C.-W. conducted XRF nano-tomography experiment at HXN beamline with the support of other group members. C. Z. and X. H. reconstructed the tomographic images. X. H. provided methods and software for quantitative analysis of XRF images. C. Z., C.-H. L. and Y.-c. K. C.-W. conducted synchrotron diffraction experiments with the XPD beamline support by J. B., H. Z. and S. G.; C. Z. conduct diffraction analysis under the guidance of J. B., X. L. and C. Z. under the guidance of X. T. to conduct XPS measurement and analysis. C. Z., X. L., and Y.-c. K. C.-W. conducted the XAS experiment at BMM beamline. C. Z., L. Y., X. L., conducted XANES and EXAFS analysis under the guidance of Y.-c. K. C.-W and C.-H. L., C. Z. and Y.-c. K. C.-W. wrote the manuscript, with inputs from other co-authors.

Conflicts of interest

The authors declare that they have no competing interests.

Acknowledgements

This material is based on work supported by the National Science Foundation under Grant No. DMR-1752839. Karen Chen-Wiegart acknowledges the support provided *via* the Faculty Early Career Development Program (CAREER) program and the Metals and Metallic Nanostructures Program of the National Science Foundation. This research used resources, Hard X-ray Nanoprobe (HXN) beamline (3-ID), Beamline for Materials Measurement (BMM) (6-BM) and X-ray Powder Diffraction (XPD) beamline (28-ID-2) of the National Synchrotron Light Source II, a U.S. Department of Energy (DOE) Office of Science User Facility operated for the DOE Office of Science by Brookhaven National Laboratory under Contract No. DE-SC0012704. This research used resources of the Center for Functional Nanomaterials (CFN), which is a U.S. DOE Office of Science Facility, at Brookhaven National Laboratory under Contract No. DE-SC0012704. Chonghang Zhao and Karen Chen-Wiegart thank Joint Photon Science Institute at Stony Brook University, which provides partial support for Chonghang Zhao *via* a student fellowship, jointly proposed by Karen Chen-Wiegart as PI and Yong Chu as co-PI and Juergen Thieme and Wah-Keat Lee as collaborators. The authors are grateful to Dr Bruce Ravel (National Institute of Standards and Technology), a scientist at BMM beamline, for his expertise and support on XANES characterization as well as his insights on data analysis and scientific interpretation. We thank the support provided by the CFN staff, Fernando

Published on 10 August 2021. Downloaded by BNL Research Library on 9/30/2021 3:33:17 PM.

Camino and Gwen Wright for the access and training on FIB-SEM and SEM/EDS. We acknowledge the support on data collection and preliminary analysis during the HXN and XPD beamtime provided by the Chen-Wiegart group members, Lijie Zou and Qingkun Meng. Lin-Chieh Yu thanked Yang Liu from Prof. Anatoly Frenkel's group at Stony Brook University and Brookhaven National Laboratory for the helpful advice on the EXAFS analysis, as well as the introduction to EXAFS analysis provided by Prof. Anatoly Frenkel through helpful discussions and the XAFS 2020 Short Course on X-ray Absorption Fine Structure. We also thank Varun Kankanallu for proofreading the manuscript.

References

1 X. Liu, M. He, D. Calvani, H. Y. Qi, K. Gupta, H. J. M. de Groot, G. J. A. Sevink, F. Buda, U. Kaiser and G. F. Schneider, *Nat. Nanotechnol.*, 2020, **15**(4), 307–312, DOI: 10.1038/s41565-020-0641-5.

2 B. Zugic, L. C. Wang, C. Heine, D. N. Zakharov, B. A. J. Lechner, E. A. Stach, J. Biener, M. Salmeron, R. J. Madix and C. M. Friend, *Nat. Mater.*, 2017, **16**(5), 558–564, DOI: 10.1038/nmat4824.

3 S. Shi, Y. Li, B.-N. Ngo-Dinh, J. Markmann and J. Weissmuller, *Science*, 2021, **371**(6533), 1026–1033, DOI: 10.1126/science.abd9391.

4 L. F. Zou, P. H. Cao, Y. K. Lei, D. Zakharov, X. H. Sun, S. D. House, L. L. Luo, J. Li, Y. Yang, Q. Y. Yin, X. B. Chen, C. R. Li, H. L. Qin, E. A. Stach, J. C. Yang, G. F. Wang and G. W. Zhou, *Nat. Commun.*, 2020, **11**(1), 3934, DOI: 10.1038/s41467-020-17826-w.

5 L. L. Huang, M. Liu, H. X. Lin, Y. B. Xu, J. S. Wu, V. P. Dravid, C. Wolverton and C. A. Mirkin, *Science*, 2019, **365**(6458), 1159–1163, DOI: 10.1126/science.aax5843.

6 C. Zhu, Z. Qi, V. A. Beck, M. Luneau, J. Lattimer, W. Chen, M. A. Worsley, J. C. Ye, E. B. Duoss, C. M. Spadaccini, C. M. Friend and J. Biener, *Sci. Adv.*, 2018, **4**(8), eaas9459, DOI: 10.1126/sciadv.aas9459.

7 A. Wittstock, V. Zielasek, J. Biener, C. M. Friend and M. Baumer, *Science*, 2010, **327**(5963), 319–322, DOI: 10.1126/science.1183591.

8 A. Pavlisic, P. Jovanovic, V. S. Selih, M. Sala, M. Bele, G. Drazic, I. Arcon, S. Hocevar, A. Kokalj, N. Hodnik and M. Gaberscek, *ACS Catal.*, 2016, **6**(8), 5530–5534, DOI: 10.1021/acscatal.6b00557.

9 A. A. El-Zoka, S. H. Kim, S. Deville, R. C. Newman, L. T. Stephenson and B. Gault, *Sci. Adv.*, 2020, **6**(49), eabd6324, DOI: 10.1126/sciadv.abd6324.

10 J. T. Zhang and C. M. Li, *Chem. Soc. Rev.*, 2012, **41**(21), 7016–7031, DOI: 10.1039/c2cs35210a.

11 W. L. An, B. A. Gao, S. X. Mei, B. Xiang, J. J. Fu, L. Wang, Q. B. Zhang, P. K. Chu and K. F. Huo, *Nat. Commun.*, 2019, **10**, 1447, DOI: 10.1038/s41467-019-09510-5.

12 Y. Q. Li, H. Shi, S. B. Wang, Y. T. Zhou, Z. Wen, X. Y. Lang and Q. Jiang, *Nat. Commun.*, 2019, **10**, 4292, DOI: 10.1038/s41467-019-12274-7.

13 Q. Chen and K. Sieradzki, *Nat. Mater.*, 2013, **12**(12), 1102–1106, DOI: 10.1038/nmat3741.

14 J. Erlebacher, M. J. Aziz, A. Karma, N. Dimitrov and K. Sieradzki, *Nature*, 2001, **410**(6827), 450–453, DOI: 10.1038/35068529.

15 N. Badwe, X. Chen, D. K. Schreiber, M. J. Olszta, N. R. Overman, E. K. Karasz, A. Y. Tse, S. M. Bruemmer and K. Sieradzki, *Nat. Mater.*, 2018, **17**(10), 887–893, DOI: 10.1038/s41563-018-0162-x.

16 J. Snyder, T. Fujita, M. W. Chen and J. Erlebacher, *Nat. Mater.*, 2010, **9**, 904–907, DOI: 10.1038/nmat2878.

17 T. Fujita, P. F. Guan, K. McKenna, X. Y. Lang, A. Hirata, L. Zhang, T. Tokunaga, S. Arai, Y. Yamamoto, N. Tanaka, Y. Ishikawa, N. Asao, J. Erlebacher and M. W. Chen, *Nat. Mater.*, 2012, **11**(9), 775–780, DOI: 10.1038/nmat3391.

18 T. Wada, K. Yubuta, A. Inoue and H. Kato, *Mater. Lett.*, 2011, **65**(7), 1076–1078, DOI: 10.1016/j.matlet.2011.01.054.

19 C. Zhao, T. Wada, V. De Andrade, G. J. Williams, J. Gelb, L. Li, J. Thieme, H. Kato and Y.-C. K. Chen-Wiegart, *ACS Appl. Mater. Interfaces*, 2017, **9**(39), 34172–34184, DOI: 10.1021/acsami.7b04659.

20 T. Wada and H. Kato, *Scr. Mater.*, 2013, **68**(9), 723–726, DOI: 10.1016/j.scriptamat.2013.01.011.

21 T. Wada, T. Ichitsubo, K. Yubuta, H. Segawa, H. Yoshida and H. Kato, *Nano Lett.*, 2014, **14**(8), 4505–4510, DOI: 10.1021/nl501500g.

22 I. V. Okulov, S. V. Lamaka, T. Wada, K. Yubuta, M. L. Zheludkevich, J. Weissmüller, J. Markmann and H. Kato, *Nano Res.*, 2018, **11**(12), 6428–6435, DOI: 10.1007/s12274-018-2167-9.

23 S. G. Yu, K. Yubuta, T. Wada and H. Kato, *Carbon*, 2016, **96**, 403–410, DOI: 10.1016/j.carbon.2015.09.093.

24 M. Tsuda, T. Wada and H. Kato, *J. Appl. Phys.*, 2013, **114**(11), 113503, DOI: 10.1063/1.4821066.

25 T. Wada, A. D. Setyawan, K. Yubuta and H. Kato, *Scr. Mater.*, 2011, **65**(6), 532–535, DOI: 10.1016/j.scriptamat.2011.06.019.

26 S. H. Joo, J. W. Bae, W. Y. Park, Y. Shimada, T. Wada, H. S. Kim, A. Takeuchi, T. J. Konno, H. Kato and I. V. Okulov, *Adv. Mater.*, 2020, **32**(6), 1906160, DOI: 10.1002/adma.201906160.

27 C. H. Zhao, T. Wada, V. De Andrade, D. Gursoy, H. Kato and Y. C. K. Chen-Wiegart, *Nano Energy*, 2018, **52**, 381–390, DOI: 10.1016/j.nanoen.2018.08.009.

28 G. Zhao, L. Zhang, Y. Niu and K. Sun, *Electrochim. Acta*, 2017, **224**, 64–70, DOI: 10.1016/j.electacta.2016.12.033.

29 T. Wada, J. Yamada and H. Kato, *J. Power Sources*, 2016, **306**, 8–16, DOI: 10.1016/j.jpowsour.2015.11.079.

30 D. Yalong, H. Hongsen, W. Hong, K. Jianli and L. Jianxin, *Mater. Res. Express*, 2019, **6**(11), 115534–115534, DOI: 10.1088/2053-1591/ab4abe.

 This journal is © The Royal Society of Chemistry 2021

Published on 10 August 2021. Downloaded by BNL Research Library on 9/30/2021 3:33:17 PM.

31 I. V. Okulov, J. Weissmuller and J. Markmann, *Sci. Rep.*, 2017, **7**, 20, DOI: 10.1038/s41598-017-00048-4.
32 L. J. Zou, M. Y. Ge, C. H. Zhao, Q. K. Meng, H. Wang, X. Y. Liu, C. H. Lin, X. H. Xiao, W. K. Lee, Q. Shen, F. Chen and Y. C. K. Chen-Wiegart, *ACS Appl. Mater. Interfaces*, 2020, **12**(2), 2793–2804, DOI: 10.1021/acsami.9b16392.
33 T. Wada, P. A. Geslin and H. Kato, *Scr. Mater.*, 2018, **142**, 101–105, DOI: 10.1016/j.scriptamat.2017.08.038.
34 A. Chuang and J. Erlebacher, *Materials*, 2020, **13**(17), 3706, DOI: 10.3390/ma13173706.
35 I. McCue, B. Gaskey, P. A. Geslin, A. Karma and J. Erlebacher, *Acta Mater.*, 2016, **115**, 10–23, DOI: 10.1016/j.actamat.2016.05.032.
36 P. A. Geslin, I. McCue, B. Gaskey, J. Erlebacher and A. Karma, *Nat. Commun.*, 2015, **6**, 8, DOI: 10.1038/ncomms9887.
37 T. Wada, K. Yubuta and H. Kato, *Scr. Mater.*, 2016, **118**, 33–36, DOI: 10.1016/j.scriptamat.2016.03.008.
38 Y. Shi, L. X. Lian, Y. Liu and N. Y. Xing, *Appl. Phys. A: Mater. Sci. Process.*, 2019, **125**(10), 685, DOI: 10.1007/s00339-019-2984-z.
39 C. H. Zhao, K. Kisslinger, X. J. Huang, M. Lu, F. Camino, C. H. Lin, H. F. Yan, E. Nazaretski, Y. Chu, B. Ravel, M. Z. Liu and Y. C. K. Chen-Wiegart, *Mater. Horiz.*, 2019, **6**(10), 1991–2002, DOI: 10.1039/c9mh00669a.
40 I. McCue and M. J. Demkowicz, *Jom*, 2017, **69**(11), 2199–2205, DOI: 10.1007/s11837-017-2571-8.
41 J. W. Kim, M. Tsuda, T. Wada, K. Yubuta, S. G. Kim and H. Kato, *Acta Mater.*, 2015, **84**, 497–505, DOI: 10.1016/j.actamat.2014.11.002.
42 J. Erlebacher, *J. Electrochem. Soc.*, 2004, **151**(10), C614–C626, DOI: 10.1149/1.1784820.
43 F. Kertis, J. Snyder, L. Govada, S. Khurshid, N. Chayen and J. Erlebacher, *Jom*, 2010, **62**(6), 50–56, DOI: 10.1007/s11837-010-0087-6.
44 Y. Sun, S. A. Burger and T. J. Balk, *Philos. Mag.*, 2014, **94**(10), 1001–1011, DOI: 10.1080/14786435.2013.876113.
45 M. M. Biener, J. Biener, A. Wichmann, A. Wittstock, T. F. Baumann, M. Baumer and A. V. Hamza, *Nano Lett.*, 2011, **11**(8), 3085–3090, DOI: 10.1021/nl200993g.
46 J. Biener, E. Farfan-Arribas, M. Biener, C. M. Friend and R. J. Madix, *J. Chem. Phys.*, 2005, **123**(9), 094705, DOI: 10.1063/1.1999607.
47 K. Holloway and P. M. Fryer, *Appl. Phys. Lett.*, 1990, **57**(17), 1736–1738, DOI: 10.1063/1.104051.
48 V. Bilovol, S. Ferrari, D. Derewnicka and F. D. Saccone, *Mater. Chem. Phys.*, 2014, **146**(3), 269–276, DOI: 10.1016/j.matchemphys.2014.03.021.
49 S. Q. Wei, Z. G. Li, S. L. Yin, X. Y. Zhang, W. H. Liu and X. G. Wang, *J. Synchrotron Radiat.*, 2001, **8**, 566–568, DOI: 10.1107/s0909049500018070.
50 N. Umesaki, N. Kamijo, I. Tanaka and K. Niihara, *Jpn. J. Appl. Phys.*, 1993, **32**, 649–651, DOI: 10.7567/jjaps.32s2.649.
51 K. Nonaka, T. Sakazawa and H. Nakajima, *Mater. Trans. JIM*, 1995, **36**(12), 1463–1466, DOI: 10.2320/matertrans1989.36.1463.
52 A. Pratap, K. N. Lad, T. L. S. Rao, P. Majmudar and N. S. Saxena, *J. Non-Cryst. Solids*, 2004, **345**, 178–181, DOI: 10.1016/j.jnoncrysol.2004.08.018.
53 J. H. Dai, B. Jiang, J. Y. Zhang, Q. S. Yang, Z. T. Jiang, H. W. Dong and F. S. Pan, *J. Phase Equilib. Diffus.*, 2015, **36**(6), 613–619, DOI: 10.1007/s11669-015-0417-z.
54 G. Liu, Y. Q. Yang, X. Luo, B. Huang and P. T. Li, *RSC Adv.*, 2017, **7**(83), 52595–52603, DOI: 10.1039/c7ra10510j.
55 R. P. Kolli and A. Devaraj, *Metals*, 2018, **8**(7), DOI: 10.3390/met8070506.
56 A. Lopez-Suarez, J. Rickards and R. Trejo-Luna, *Int. J. Hydrogen Energy*, 2003, **28**(10), 1107–1113, DOI: 10.1016/s0360-3199(02)00202-1.
57 M. H. F. Sluiter, *Phase Transitions*, 2007, **80**(4–5), 299–309, DOI: 10.1080/01411590701228562.
58 A. Anastasopol, T. V. Pfeiffer, J. Middelkoop, U. Lafont, R. J. Canales-Perez, A. Schmidt-Ott, F. M. Mulder and S. W. H. Eijt, *J. Am. Chem. Soc.*, 2013, **135**(21), 7891–7900, DOI: 10.1021/ja3123416.
59 K. Asano, H. Enoki and E. Akiba, *J. Alloys Compd.*, 2009, **480**(2), 558–563, DOI: 10.1016/j.jallcom.2009.01.086.
60 A. Takeuchi and A. Inoue, *Mater. Trans.*, 2005, **46**(12), 2817–2829, DOI: 10.2320/matertrans.46.2817.
61 A. Manzoor, S. Pandey, D. Chakraborty, S. R. Phillpot and D. S. Aidhy, *npj Comput. Mater.*, 2018, **4**, 47, DOI: 10.1038/s41524-018-0102-y.
62 D. B. Miracle and O. N. Senkov, *Acta Mater.*, 2017, **122**, 448–511, DOI: 10.1016/j.actamat.2016.08.081.
63 F. M. Zhang, L. L. Wang, P. Li, S. L. Liu, P. P. Zhao, G. Dai and S. Y. He, *Adv. Eng. Mater.*, 2017, **19**(2), 1600600, DOI: 10.1002/adem.201600600.
64 H. Feufel and F. Sommer, *J. Alloys Compd.*, 1995, **224**(1), 42–54, DOI: 10.1016/0925-8388(95)01526-4.
65 H. Wu, T. Mayeshiba and D. Morgan, *Sci. Data*, 2016, **3**, 160054, DOI: 10.1038/sdata.2016.54.
66 Y. C. K. Chen-Wiegart, F. E. Camino and J. Wang, *ChemPhysChem*, 2014, **15**(8), 1587–1591, DOI: 10.1002/cphc.201400023.
67 E. Nazaretski, H. Yan, K. Lauer, N. Bouet, X. Huang, W. Xu, J. Zhou, D. Shu, Y. Hwu and Y. S. Chu, *J. Synchrotron Radiat.*, 2017, **24**, 1113–1119, DOI: 10.1107/s1600577517011183.
68 L. Li, H. Yan, W. Xu, D. T. Yu, A. Heroux, W. K. Lee, S. I. Campbell and Y. S. Chu, In PyXRF: Python-Based X-ray Fluorescence Analysis Package, Conference on X-Ray Nanoimaging - Instruments and Methods III, San Diego, CA, Aug 07-08, San Diego, CA, 2017.
69 M. D. Hanwell, C. J. Harris, A. Genova, J. Schwartz, Y. Jiang and R. Hovden, *Microsc. Microanal.*, 2019, **25**, 408–409, DOI: 10.1017/S1431927619002770.
70 C. A. Schneider, W. S. Rasband and K. W. Eliceiri, *Nat. Methods*, 2012, **9**(7), 671–675, DOI: 10.1038/nmeth.2089.

71 P. Thevenaz, U. E. Ruttimann and M. Unser, *IEEE Trans. Image Process.*, 1998, **7**(1), 27–41, DOI: 10.1109/83.650848.
72 D. Gürsoy, F. De Carlo, X. Xiao and C. Jacobsen, *J. Synchrotron Radiat.*, 2014, **21**(5), 1188–1193, DOI: 10.1107/S1600577514013939.
73 A. O'Mara, A. E. King, J. C. Vickers and M. T. K. Kirkcaldie, *J. Open Res. Softw.*, 2017, **5**(1), 31, DOI: 10.5334/jors.172.
74 B. Munch and L. Holzer, *J. Am. Ceram. Soc.*, 2008, **91**(12), 4059–4067, DOI: 10.1111/j.1551-2916.2008.02736.x.
75 X. Y. Liu, D. Vonk, H. Jiang, K. Kisslinger, X. Tong, M. Y. Ge, E. Nazaretski, B. Ravel, K. Foster, S. Petrash and Y. C. K. Chen-Wiegart, *ACS Appl. Nano Mater.*, 2019, **2**(4), 1920–1929, DOI: 10.1021/acsanm.8b02309.
76 B. Ravel and M. Newville, *J. Synchrotron Radiat.*, 2005, **12**, 537–541, DOI: 10.1107/s0909049505012719.

Published on 10 August 2021. Downloaded by BNL Research Library on 9/30/2021 3:33:17 PM.

This journal is © The Royal Society of Chemistry 2021